Check for updates

Functionalized polymer dielectrics for low-operating voltage organic field-effect transistors

John Barron[1], Jaewon Lee[2], Suchismita Guha[1,a)] (iD)

[1] *Department of Physics and Astronomy, University of Missouri, Columbia, MO 65211, USA*
[2] *Department of Chemical Engineering, University of Missouri, Columbia, MO 65211, USA*
a) Address all correspondence to this author. e-mail: guhas@missouri.edu

The design of appropriate dielectrics plays a crucial role in the performance of organic field-effect transistors (FETs). Along with the active semiconductor layer, the dielectric–semiconductor interface governs charge transport properties in FETs. A viable route for enhancing the dielectric constant of polymer dielectrics is via the incorporation of semiconducting and insulating nanoparticles. Magnetic nanocrystals such as cobalt ferrite (CFO) have received a lot of interest in sensing and biomedical applications. Its insulating property is attractive in polymer gate dielectrics. CFO magnetic nanocrystals, soluble in organic solvents, were synthesized by a thermal decomposition method and coated with poly(vinyl alcohol). Improved performance of organic FETs using CFO-incorporated non-ferroelectric dielectrics is observed. In particular, the threshold voltage and the subthreshold swing are lowered in pentacene FETs using CFO-incorporated cross-linked poly(4-vinyl phenol) dielectric. The application of an external magnetic field allows for another parameter to tune the device performance.

Introduction

There has been a lot of improvement in the performance of organic field-effect transistors (FETs) over the past two decades. Organic FETs, which are the building blocks of electronic circuits, find numerous applications in wearable electronics for healthcare and implantable electronics [1–3]. The charge carrier mobility, an important performance metric, in organic FETs has increased by orders of magnitudes in the last two decades from 10^{-5} to 10^{-6} cm^2/Vs in the early 1990s to over 10 cm^2/Vs [4]. Because the semiconductor–dielectric interface governs charge transport mechanisms in FET architectures, achieving intrinsic carrier mobility specific to a semiconductor is challenging. The dielectric layer not only influences the morphology of the semiconducting layer but it may also affect the density of states (DOS) due to local polarization effects [5–7]. Polarizable gate dielectrics, for example, broaden the DOS at the semiconductor–dielectric interface due to charge–dipole coupling, increasing the localization of carriers at the interface. This inherently means that low κ (dielectric constant) dielectrics in organic FETs achieve better performance compared to high κ dielectrics. However, since majority of organic FETs operate in the accumulation region, the operating voltages of FETs with low

κ dielectrics are high due to the low capacitance ($C \propto \kappa$). Low-operating voltage organic FETs still remain a challenge since it entails high κ (organic or inorganic) dielectrics. Such dielectrics emphasize dynamic coupling of the charge carriers to the electronic polarization at the semiconductor–dielectric interface as a result of the Fröhlich interaction [8, 9]. Due to this interaction, there is a decrease in the charge carrier mobility, which can be understood on the basis of a renormalization of the transfer integral and an increase in the effective mass of the carriers [10].

Working to achieve low-operating voltage organic FETs, our prior work has utilized polymer ferroelectric dielectrics based on polyvinylidene fluoride (PVDF). In particular, the copolymer, PVDF-TrFE (75:25) has a tunable κ with temperature; the room temperature value is: 8. Using 120-nm-thick PVDF-TrFE films, the operating voltages for TIPS-pentacene FETs were found to be less than 2 V [11]. Further, we have been able to reduce the dipolar disorder at the semiconductor–dielectric interface by judiciously combining vertical and lateral poling of the PVDF-TrFE layer, referred to as textured poling. For p-type FETs, a negative poling in the vertical direction near the semiconductor interface improves charge accumulation. In TIPS-pentacene/PVDF-TrFE FETs, textured poling yields carrier mobilities > 1

cm^2/Vs with high on/off ratios [12]. However, one drawback with this method is that only bottom gate FET architectures may be realized. Furthermore, the method of electrical poling involves additional steps after depositing the ferroelectric dielectric layer.

Adding insulating nanoparticles in a controlled fashion to any dielectric layer, in particular, magnetic nanoparticles such as cobalt ferrite, has the benefit of enhancing the capacitance without affecting the localization of carriers at the interface. An added advantage of such a strategy is that it provides a mechanism for tuning charge transport in organic FETs via external magnetic fields. Metal-doped nanoparticles of spinel MFe_2O_4, where M is a + 2 cation of Mn, Fe, Co, or Ni, have received a lot of attention as contrast agents for magnetic resonance imaging [13]. In particular, cobalt ferrite ($CoFe_2O_4$ or CFO), owing to its moderate values of saturation magnetization, high magneto-crystalline anisotropy, high Curie temperature, and easy tunability of particle size [14, 15] is used in biomedical applications [16–19]. Furthermore, CFO is attractive for use as a gate dielectric in organic FETs due to its insulating properties, making magnetic field-controlled transistors and devices a viable possibility [20]. Zang et al. demonstrated gate engineering in flexible organic FETs by using Fe_3O_4 nanoparticles-incorporated silver nanowires as the gate electrode [21]. These flexible FETs show a dramatic change (increase in current) in the transistor transfer characteristics when a small field of 150 mT is applied upon deformation, mainly due to the magnetic force acting on the gate electrode.

CFO nanoparticles tethered to self-assembled peptide nanostructures have provided a platform for tuning the magnetic properties as well as providing a viable route towards using it as a dielectric in organic FETs. In particular, the operating voltage of pentacene FETs with CFO-embedded peptide nanostructures as a gate dielectric layer is substantially lower compared to using only peptide nanostructures as a dielectric layer of similar thickness [22]. However, the roughness and the non-uniformity of peptide nanostructured films often result in gate leakage current in FETs. We point out that the peptide nanostructures are also ferroelectric, inducing polarization effects at the semiconductor–insulator interface. Moving forward, we combine CFO with promising non-ferroelectric dielectrics such as cross-linked poly (4-vinyl phenol) (PVP) in FET architectures.

Here, we explore the performance of organic FETs using CFO-embedded cross-linked PVP. We have used both commercially obtained CFO nanoparticles (~ 20 nm) as well as CFO nanoparticles synthesized by a thermal decomposition method and coated with poly(vinyl alcohol) (PVA) (~ 5 nm). Capacitance versus frequency (C–F) and capacitance versus voltage (C–V) measurements were conducted from metal–insulator–metal (MIM) and metal–insulator–semiconductor (MIS) diodes. For the same thickness of the PVP dielectric layer, we find a higher value of capacitance when CFO nanoparticles are embedded. The clustering issue in neat CFO nanoparticles is mitigated by PVA-coated CFO nanoparticles. The functionalized dielectrics were further used in pentacene FETs. Compared to as-is PVP dielectric, the addition of CFO nanoparticles to the dielectric layer is seen to improve the on/off ratio of the FET along with reducing the operating voltage. Moreover, upon the application of a small magnetic field, a change in the FET transfer characteristics was observed.

Results and discussion

Structure, morphology, and magnetic property of CFO- and PVA-coated CFO nanoparticles

CFO, which belongs to the iron oxide (Fe_3O_4) group with ferrimagnetic spin structure, is a partially inverse spinel structure. A perfect spinel structure has 24 cations (of A^{2+} and B^{3+} type) occupying 8 of the 64 available tetrahedral (T_d) sites and 16 of the 32 available octahedral (O_h) sites in addition to the 32 oxygen anions. For a perfect inverse spinel structure, half of the B^{3+} occupy the T_d sites, and 8 A^{2+} ions and 8 B^{3+} ions occupy the O_h sites. The structure of Fe_3O_4 with the O_h and T_d sites is represented in Fig. 1(a). Fe^{2+} and Fe^{3+} ions occupying the O_h sites align parallel to an external magnetic field and Fe^{3+} ions in the T_d lattice sites align antiparallel to the field [23], as depicted by the blue and black arrows. The Co ions in CFO mainly occupy the O_h site, replacing the Fe^{2+} ions. In the perfect case, $(Fe^{3+})_{Td}$ $(Co^{2+}, Fe^{3+})_{Oh}$, the spins of Fe^{3+} in the O_h and the T_d sites would cancel, leaving only the Co^{2+} to contribute. From the effective Bohr magneton: $g[J(J + 1)]^{1/2}$, where J is the total angular momentum and g is the Landé g-factor, the effective magnetic moment (μ_B) per ion for Co^{2+} ($3d^7$) is 3.87. A higher or a lower value of the saturation magnetization compared to 3.87 suggests the occupation of some T_d sites by Co ions such that a complete cancelation of spins by the Fe^{3+} ions is not achieved.

Details of magnetization properties for the neat CFO used in this work are provided in Ref. [22]. Since the nanoparticles lack any domain structure, the magnetization curve obtained for CFO is representative of superparamagnetism with a low coercive field [Fig. 1(b)]. The CFO nanoparticles exhibit a saturation magnetization of 3.6 μ_B/formula unit, slightly lower than the theoretical value. The x-ray diffraction (XRD) analysis had further shown that 70% of the Co ions are in the O_h site, accounting for the lower value of the saturation magnetization compared to the theoretical estimate. More recently, single-crystal-like CFO thin films have been achieved with a new bilayer growth method, showing large hysteresis in the magnetization curves along with large magnetic coercivity [24]. The XRD pattern for the synthesized CFO nanocrystals was further measured; it is demonstrated as an inverse spinel structure as shown in Fig. 1(c).
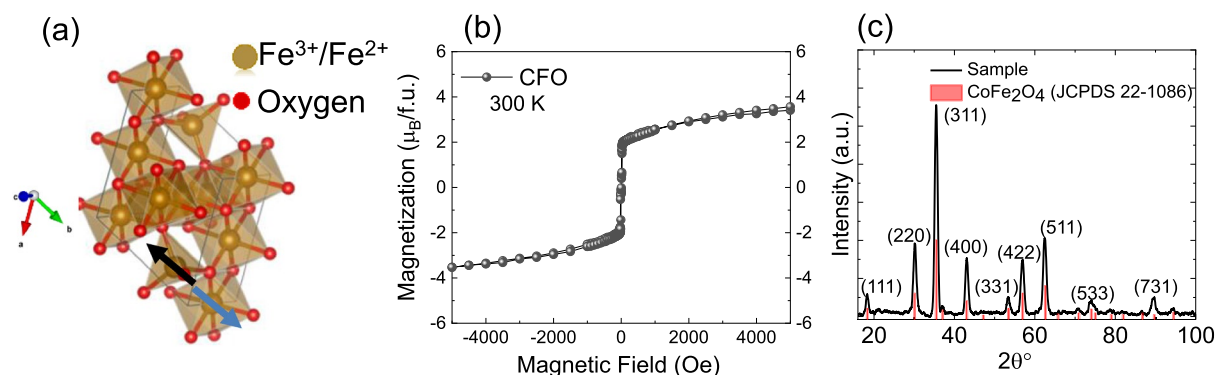
Figure 1: (a) Crystal structure of Fe_3O_4, where the Fe^{3+} ions occupy both the T_d and O_h sites, and the Fe^{2+} ions occupy the O_h sites. The black and the blue arrows depict the direction of the magnetic moment of Fe ion on the T_d and O_h sites, respectively. In CFO, the Co^{2+} ions replace the Fe^{2+} ions in the O_h site. (b) Magnetization hysteresis curve for as-is CFO nanoparticles at room temperature. (c) XRD pattern of CFO nanocrystals and standard CFO (JCPDS 22–1086).

Along with neat CFO, PVA-coated CFO was synthesized by a thermal decomposition method [25]. Details are provided in the Experimental Methods section. Figure 2 shows a schematic of the synthesis process. The first step involves the synthesis of CFO nanoparticles in a solvent. Figure 2(b) illustrates the attraction of CFO nanoparticles dispersed in chloroform to a bar magnet. The second step involves the coating of CFO nanoparticles with PVA, as schematically shown in Fig. 2(c). This method allows the coated CFO nanoparticles to be dispersed in typical solvents such

as dimethyl fluoride (DMF) used for dissolving polymer dielectrics.

The TEM images of the CFO nanocrystals in chloroform and the ones coated with PVA in DMF are shown in Fig. 3(a) and (b), respectively. The particle size is approximately 5 nm. The CFO nanocrystals coated with PVA were dispersed individually and no aggregates were observed. It suggests that PVA coating can improve the colloidal stability in DMF, leading to uniformly distributed CFO nanocrystal in the film. To quantify the CFO nanocrystals in cPVP:CFO films of the prepared
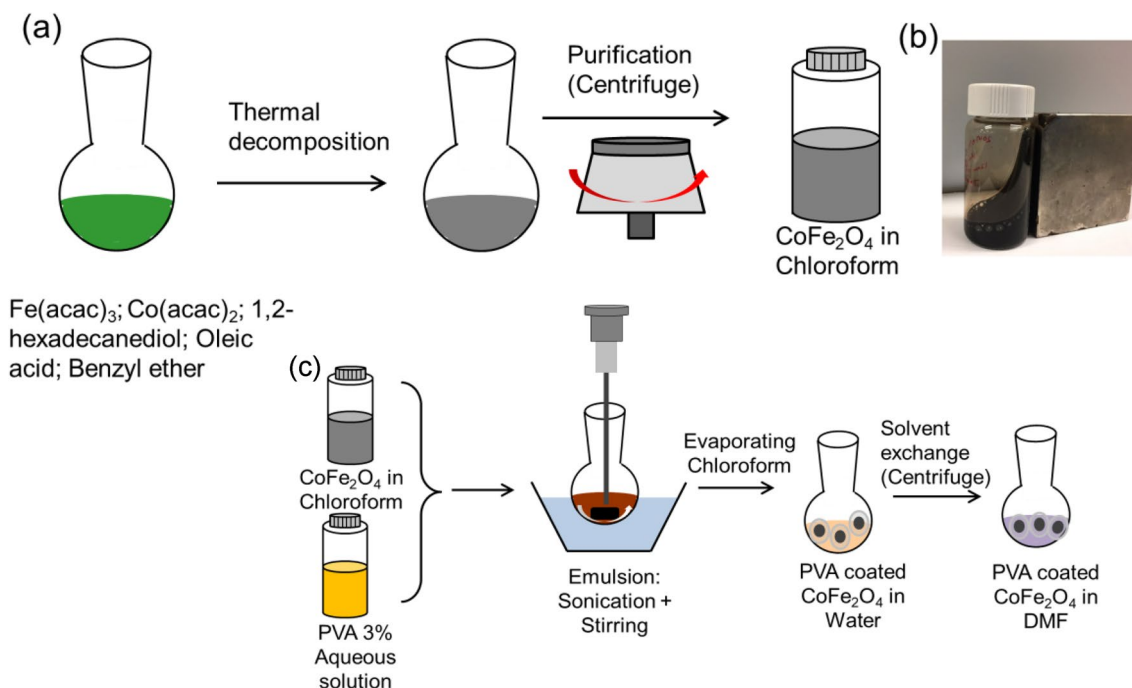

Figure 2: (a) Scheme of synthesis of CFO nanoparticles in chloroform by thermal decomposition. (b) Attraction of CFO dispersion by an external bar magnet. (c) Scheme for the synthesis of PVA-coated CFO nanoparticles in DMF.
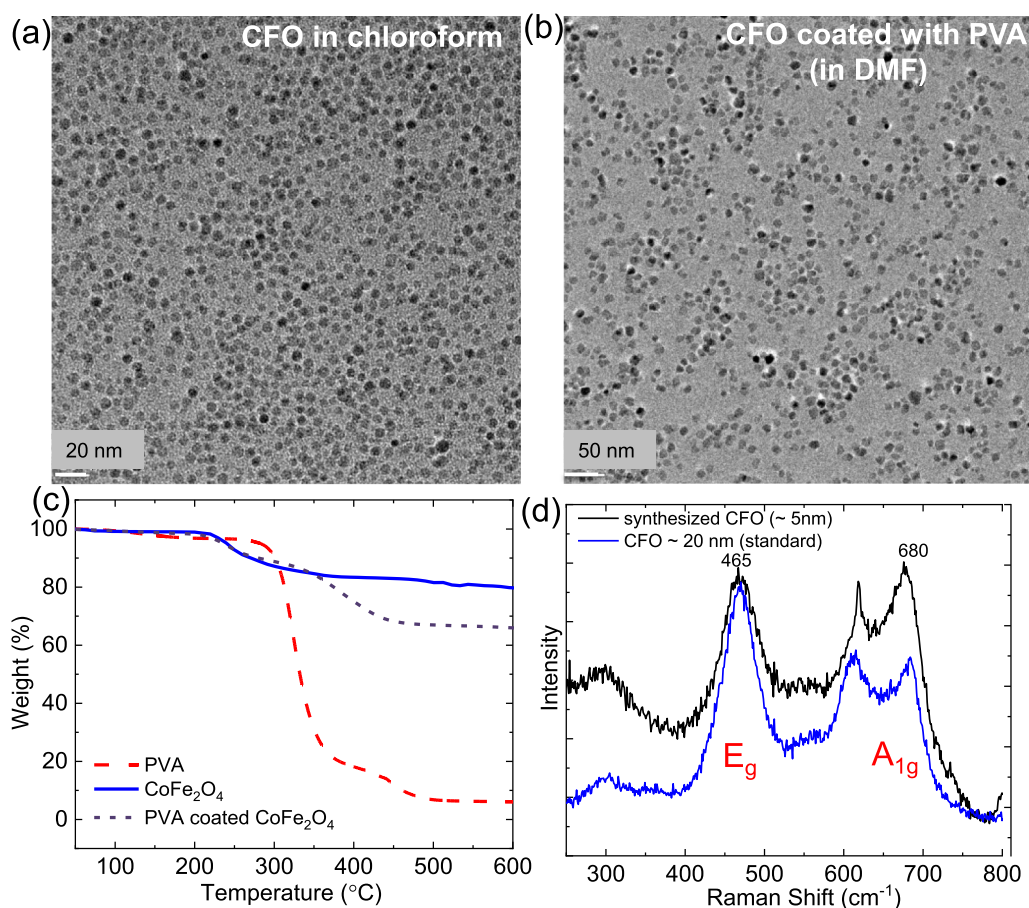
Figure 3: (a) TEM image of CFO nanocrystals synthesized by thermal decomposition. (b) TEM image of CFO nanocrystals coated with PVA in DMF solvent. (c) TGA curves for PVA, CFO, and PVA-coated CFO. (d) A comparison of Raman spectra from neat CFO and synthesized CFO.

FETs, the weight ratio of oleic acid to CFO nanocrystals and PVA to CFO nanocrystals was characterized by thermal gravimetric analysis (TGA). Figure 3(c) shows the weight losses, which occurred at two steps during the heating of PVA–CFO nanocrystals. The first weight loss began at 230 ℃ and continued to about 350℃, which likely corresponded to the degradation of oleic acid. This degradation pattern exactly agreed with the observation of the oleic acid-coated CFO nanocrystals (no PVA on the CFO nanocrystal surface). The weight loss analysis of pristine oleic acid could not be conducted because the liquid phase of oleic acid cannot be mounted in the TGA instrument. The second weight loss was revealed at about 400 ℃, which corresponds to the degradation of PVA. This degradation pattern follows the PVA thermal degradation profile. The weight loss of oleic acid exhibited 13.5%, and a 20.2% PVA weight loss was observed. Based on the measured weight ratio of organic compounds to PVA nanocrystal, the CFO concentration in DMF was determined.

The Raman scattering spectra from the synthesized CFO nanocrystals are compared with the commercially obtained neat CFO nanoparticles (− 20 nm), as shown in Fig. 3(d). The spinel structure of ferrites has 39 vibrational modes, out of which six phonon modes are Raman active ($2A_{1g}$, E_g, and $3T_{2g}$) [22]. The A_{1g} (1) and the E_g modes (at 680 cm^{-1} and 465 cm^{-1}, respectively) are clearly seen in the synthesized CFO nanoparticles.

MIM and MIS diodes

Polymer dielectrics such as PVP and polymethylmethacrylate (PMMA) allow the feasibility of low-operating voltage FETs with improved dielectric/semiconductor interfaces compared to oxide dielectrics such as SiO$_2$, especially if the dielectric thickness is controlled [26, 27]. The polar OH groups in PVP may result in instability of devices, especially since they are slowly re-oriented by the electric field. Our prior work has shown that both non-ferroelectric and ferroelectric dielectrics when dissolved in high dipole moment solvents such as propylene carbonate and DMF help modify the interaction between the dipoles by reorganizing the dipolar field in the polymer dielectric layer, and thus improving the performance of FET devices utilizing such layers [28, 29].

CFO-incorporated polymer dielectrics were used in both MIM and MIS structures to obtain insights into the dielectric/ capacitance properties. We used cross-linked PVP (cPVP) as the dielectric layer. MIM capacitors fabricated from as-is cPVP and 20:1 wt% cPVP:CFO films of the same thickness (50 nm) show a difference in their capacitance values [Fig. 4(b)]. The CFO nanoparticles in these films were the ones commercially obtained without any coating. It is clearly seen that the addition of CFO nanoparticles enhances κ of the dielectric matrix. By applying a small magnetic field (0.1 T) to the cPVP:CFO MIM device, the capacitance is seen to further increase [Fig. 4(c)].

There are several origins to magnetocapacitance. (a) The phenomenon of magnetocapacitance in tunneling junctions such as Pd/AlOx/Al arises due to the spin-dependent potential on electron screening lengths [30]. (b) A magneto-dielectric/ capacitance response in nanocomposites has been attributed to the interfacial polarization of the two phases [31, 32]. This usually occurs in multiferroic composites where ferroelectricity and ferromagnetism co-exist. Such films can exhibit giant magnetocapacitance values due to the large compressive stress in the CFO phase. (c) Organic semiconductors doped with spin radicals upon photoexcitation show enhanced magnetocapacitance due to an internal spin-exchange interaction [33]. The increase in magnetocapacitance at a field strength of 0.1 T [in Fig. 4(c)] is approximately 4%. One may be able to invoke the ideas in (b) to explain the behavior, although PVP is not ferroelectric. However, as shown in Fig. 5, the capacitance–voltage curves show a hysteresis, similar to what is seen in polymer ferroelectric dielectrics, signaling polarization effects. It is likely that the presence of the magnetic field results in a field-dependent structural organization, enhancing the space charge polarization and, thus, the capacitance. A similar effect was also observed with capacitors fabricated with CFO tethered to self-assembled peptide nanotubes, where the peptide nanotubes act as the dielectric layer [22].

To ascertain whether the synthesized PVA-coated CFO nanocrystals provide a similar platform for enhancing the capacitance of a polymer dielectric compared to neat CFO, we fabricated MIS diodes with pentacene as the semiconducting layer. Increasing the concentration of CFO/PVA in cPVP results in some non-uniformity of films, as shown in the optical images of spincoated films in Fig. 5(a). For the MIS and FET architectures, we choose the 16:1 (cPVP:CFO/PVA) concentration as an optimized film architecture. This concentration demonstrates uniform coverage over an area where several devices could be compared along with the goal of achieving a higher capacitance compared to as-is cPVP devices.

By sweeping the bias voltage, the capacitance changes from accumulation, depletion, and inversion of charges at the semiconductor–insulator interface. Due to the long relaxation of the minority carriers, the inversion layer is not typically observed in organic MIS diodes. The accumulation capacitance is essentially the capacitance of the dielectric layer. C–V curves from MIS diodes highlight interfacial properties at the semiconductor–dielectric interface. For identical film thicknesses, the capacitance of the MIS diode with cPVP + CFO/PVA is higher than only cPVP [Fig. 5(c)], which is again an indication that the addition of CFO/PVA in cPVP enhances κ. It is further seen that the hysteresis, which may arise due to the polarizing dipole charges of the OH group, is reduced when CFO/PVA is added.

The hysteresis that results from the polar OH group of polymers is well documented in the literature; the polar group acts as a trapping site [34]. Further, the crosslinking agent that couples the OH groups with either hydrogen or methyl groups reduces this hysteresis [35]. The further reduction in the influence of the OH groups in cPVP in our experiment can be understood based on a physical crosslinking occurring between the OH group and the oxide group of CFO nanoparticles. A similar reduction has been previously demonstrated by Beaulieu et al., who observed a noticeable decrease in hysteresis of their device characteristics as
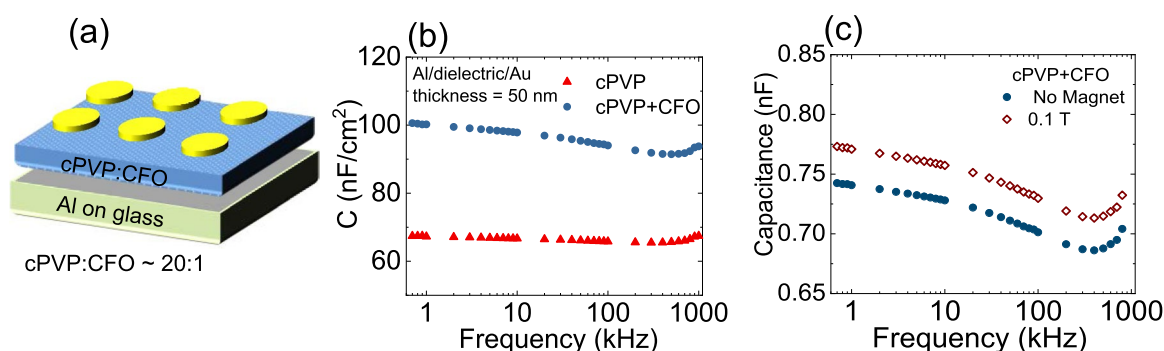

Figure 4: (a) Schematic of MIM capacitors. (b) Capacitance vs. frequency (C–F) characteristics from cPVP and cCVP + CFO MIM capacitors. (c) C–F characteristics of cCVP + CFO MIM capacitor with (0.1 T) and without magnetic field. The diameter of the Au contacts for the MIM capacitors reflected in (b) and (c) was 750 μm.
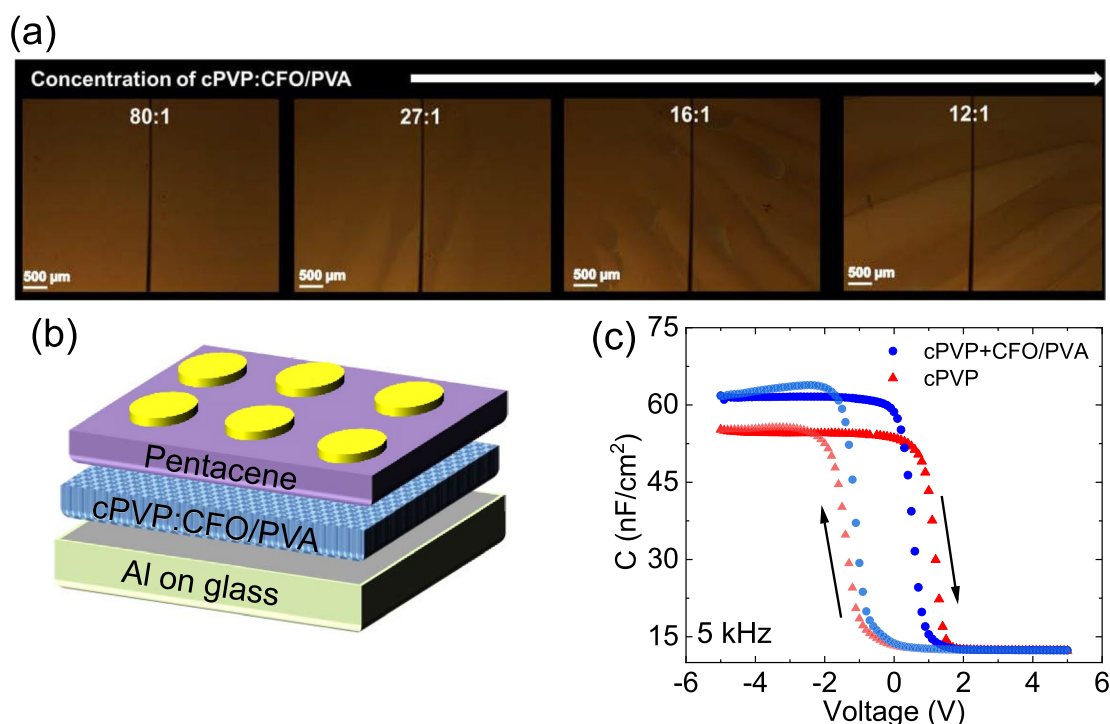
Figure 5: (a) Optical images of spincoated cPVP films as a function of PVA-coated CFO. (b) Schematic of a MIS diode. (c) Capacitance–voltage characteristics from MIS diodes with cPVP (red) and cPVP + CFO/PVA (red) dielectrics.

they increased the amount of ZrO_2 nanoparticles in their polymer layer [36].

FET characteristics

We fabricated pentacene FETs using a similar concentration of neat CFO in cPVP as used in the MIM structures (Fig. 4). The nomenclatures cPVP:CFO and cPVP + CFO/PVA refer to neat CFO and CFO/PVA nanoparticles incorporated in the dielectric layer, respectively. Typical FET characteristics (output and transfer curves) from a pentacene FET with cPVP:CFO are shown in Fig. 6(a) and (b). The transistors operate well below 2 V with a threshold voltage (V_{Th}) of approximately − 1 V. We use the saturation region of the transfer characteristics to obtain the carrier mobility (μ). In this region, $\mu = \frac{2L}{WC_i} \left(\frac{\partial \sqrt{I_{DS}}}{\partial V_{GS}} \right)^2$, where C_i is the dielectric capacitance, W is the channel width, L is the channel length, V_{GS} is the gate voltage, I_{DS} is the drain current, and V_{DS} is the drain-source voltage. Due to the non-uniformity of neat CFO nanoparticles in cPVP, using cPVP + CFO/PVA in FETs gives a higher level of control. We compare the transfer characteristics of two similar pentacene FETs: one with as-is cPVP and the other with cPVP + CFO/PVA with a specific W/L ratio in Fig. 6(c). The dielectric thicknesses were approximately the same (55 nm). These were measured from positive to negative voltages. As such, there is a small hysteresis in the transfer characteristics when sweeping the voltage from negative to positive values.

The average carrier mobilities and V_{Th} from all three dielectrics (with comparable thickness) are represented in Fig. 6(d) and (e). As observed, V_{Th} is the smallest for cPVP:CFO FET; however, due to a clustering effect with neat CFO, the on/off ratio and carrier mobility are lower compared with cPVP + CFO/PVA FETs. Although the carrier mobilities and V_{Th} are similar for cPVP and cPVP + CFO/PVA devices, the on/off ratio is enhanced by an order of magnitude with the addition of CFO/PVA; the addition of nanocrystals reduces the off current. The polarizing OH group in PVP, which results in a hysteresis of the C–V curve (Fig. 5), could induce a spontaneous polarization along the lateral direction of the FET, resulting in an increase in the off current. Similar behavior has been observed with polarizable ferroelectric dielectrics where lateral poling, which sets up a parallel spontaneous electric field, increases the off current [11]. The addition of CFO could act to reduce spontaneous polarization, consistent with the reduction in the hysteresis of the C–V curve, thereby decreasing the off current. In Table 1, we compare our device performance to other works utilizing nanoparticle–polymer composites towards enhancing the dielectric properties in FET devices.

The transfer characteristics were also measured in the presence of a small magnetic field (transverse) for as-is cPVP and cPVP + CFO/PVA pentacene FETs, as shown in Fig. 7. In the
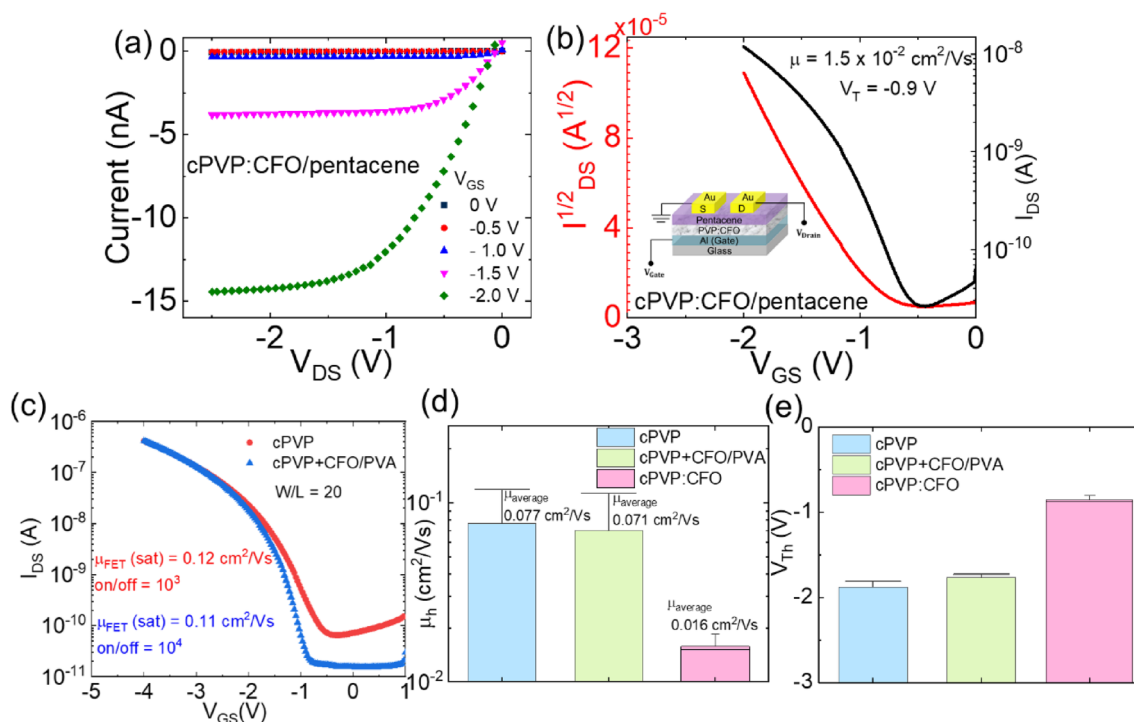
Figure 6: (a) Output and (b) transfer characteristics of cPVP:CFO/pentacene FET. The inset in (b) shows a schematic of the FET geometry. (c) Transfer characteristics of pentacene FETs with cPVP (red curve) and cPVP + CFO/PVA (blue curve) dielectrics. (d) Average carrier mobilities and (e) average threshold voltages from pentacene FETs using cPVP (blue), cPVP + CFO/PVA (green) and cPVP:CFO (pink) dielectrics.

TABLE 1: FET performance with various polymer nanocomposites.

Dielectric Polymer	Nanoparticle	Semiconductor	μ_{sat} (cm^2/Vs)	On/Off	V_{th} (V)	Reference
cPVP	CFO	Pentacene*	0.018	10^2	− 0.87	This work
cPVP	CFO/PVA	Pentacene*	0.110	10^4	− 1.75	This work
cPVP	AT/ODPA	Pentacene*	0.400	10^4	− 5.00	[37]
cPVP	AT/ODPA	F$_{16}$CuPC**	0.005	10^3	+ 2.00	[37]
cPVP	BZ	Pentacene*	0.200	10^4	− 6.00	[38]
cPVP	TiO$_2$	Pentacene*	0.105	10^3	− 0.80	[39]
PI	HfO$_2$	Pentacene*	0.110	10^4	− 6.19	[40]
PVA	Al$_2$O$_3$	CuPC*	0.057	–	–	[41]
CYLEP	ZrO$_2$	P3HT*	0.080	10^3	− 1.00	[36]

*p-type semiconductor; **n-type semiconductor; cyanoethyl pullulan (CYELP); polyimide (PI); aluminum titanate (AT); n-octadecylphosphonic acid (ODPA); barium zirconate (BZ).
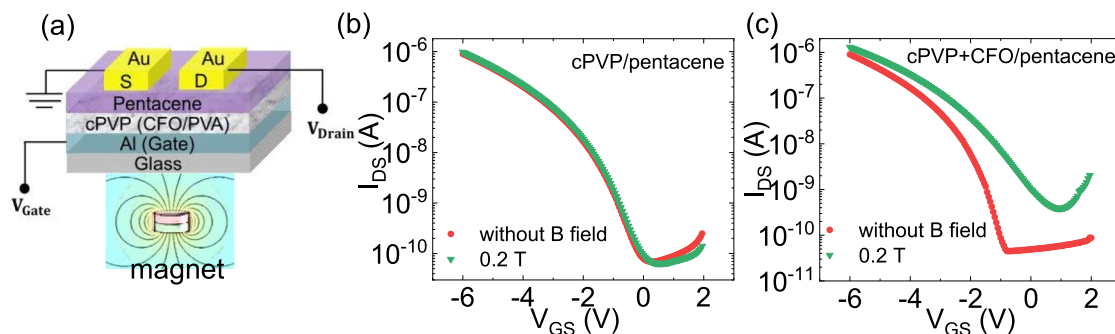

Figure 7: (a) Schematic of an organic FET in the presence of an external magnetic field. (b) Transfer characteristics of as-is cPVP/pentacene FET with and without an external magnetic field. (c) Transfer characteristics of cPVP + CFO/PVA/pentacene FET with and without an external magnetic field.

absence of CFO [Fig. 7(b)], no changes are seen in the transfer characteristics upon applying a small field. In the presence of CFO, however, I_{DS} increases with a slight increase in the off current in the presence of 0.2 T. Upon removing the field, the transfer characteristics does not completely recover, at least within half an hour, suggesting that some trapping sites may be filled/unfilled. Although the effect of the B field here seems to degrade the FET performance, with a different FET geometry and the orientation of the field, one may be able to enhance the on/off ratio.

In bendable FETs with magnetic electrodes, it has been shown that the change in the transfer characteristics (enhancement in I_{DS}) upon the application of a field (B_0) arises due to a magnetic force (F_B), where $F_B \propto B_0 \frac{dB}{dz}$; z being perpendicular to the FET in the direction of the applied field [21]. Since the distribution of the CFO nanoparticles in the dielectric layer is not completely uniform, there may be a gradient, due to which the magnetic force may influence the trap states, altering the transfer characteristics. Hence, it is conceivable that in the presence of a bending force (where the substrate itself can be bent), the change in I_{DS} under the presence of an external field is accentuated.

Conclusions

In conclusion, the addition of magnetic nanocrystals to polymer dielectrics opens up a practical route towards enhancing the dielectric constant, offering a path towards low-operating voltage organic FETs. Furthermore, the incorporation of such nanoparticles into solution-processable polymers facilitates device fabrication over large areas or on flexible surfaces through the use of spincoating, inkjet printing, or other roll-to-roll methods. CFO magnetic nanoparticles, which are very attractive for magnetic storage and biomedical applications, when embedded in polymer dielectrics such as cPVP enhance the capacitance of MIS and MIM diodes compared to as-is cPVP. PVA-coated CFO nanocrystals synthesized using a thermal decomposition method allows uniform coverage in cPVP films. In MIS structures, a reduction in the C–V hysteresis is observed with CFO/PVA-embedded cPVP, suggesting a decrease in the polarizing dipole charge due to the OH group. These dielectrics when utilized in organic FETs show higher on/off ratios compared with as-is cPVP films (without any CFO). In the presence of a weak external magnetic field, the transport properties of organic FETs can be further tuned with CFO embedded polymer dielectrics. These results open a new direction in organic electronics for magnetic field-controlled FETs. We show a proof of concept for such working FETs, which could lead to a natural extension of magneto-electric devices using CFO-incorporated ferroelectric polymer dielectrics. Future work will explore different FET geometries on flexible substrates along with varying the

orientation of the magnetic field to understand the mechanism of transport under applied fields.

Experimental methods

Materials

CFO was purchased from Inframat Advanced Materials with an average particle size of 20 nm. For the cross-linked PVP solution, poly(4-vinylphenol) (Mw = 25,000) and crosslinking agent poly(melamine-co-formaldehyde) methylated (PMMF) (84 wt% in 1-butanol) were purchased along with solvents propylene glycol monomethyl ether acetate (PGMEA) and N,N-dimethylformamide (DMF) from Sigma Aldrich. For the metal contacts used in all devices, aluminum and gold wires (99.99% purity for each) were purchased from Kurt J. Lesker. Pentacene for thermal evaporation was obtained through Tokyo Chemical Industry for use as the semiconducting layer in MIS and FET architectures. Coin-shaped neodymium magnets, which were used to apply external magnetic fields to our devices, were purchased from K&J Magnetics, Inc.

Synthesis of PVA-coated CFO

$CoFe_2O_4$ magnetic nanocrystals, soluble in organic solvents, were synthesized by a thermal decomposition method as discussed in Ref. [25]. A schematic of the process is shown in Fig. 2. Benzyl ether (20 mL) was mixed with 2 mmol of iron (III) acetylacetonate, cobalt (II) acetylacetonate (1 mmol), 10 mmol of 1,2-hexadecanediol, 6 mmol of dodecanoic acid, and 6 mmol of dodecylamine under ambient nitrogen conditions. The mixture was preheated to 150 °C for 120 min and heated to reflux at 300 °C for 30 min. The reactants were cooled to room temperature, and the products were purified with excess pure ethanol.

To prepare coated CFO, 5 mg of magnetic nanocrystals was dissolved in 10 mL of chloroform. The organic phase was added to 20 mL of an aqueous phase containing 200 mg of poly(vinyl alcohol) (PVA). After mutual saturation of the organic and continuous phase, the mixture was emulsified for 10 min with a combination of magnetic stirring (1000 rpm) and sonication (top-probe Qsonica, Model Q55 sonicator, 10 kHz,). After evaporation of the organic solvent by magnetic stirring (1000 rpm for 1 day), the products were purified by filtration and centrifuged at 11 k rpm. The precipitates were redispersed in DMF. Half of the solution was dried in the vacuum oven (100 °C under vacuum) to quantify the concentration of the PVA-coated CFO nanocrystals in DMF. The weight of the completely dried PVA-coated CFO nanocrystals was measured. The exact concentration of the prepared PVA-coated CFO nanocrystals in DMF was estimated by the following relation (CFO concentration = (the measured weight of the dried PVA-coated CFO nanocrystals × (1-weight ratio of organic compounds to the

PVA-coated CFO nanocrystals)) / the volume of DFM PVA-coated CFO nanocrystals dispersed before drying). The ratio of organic compounds to the PVA-coated CFO nanocrystals was obtained from the TGA data.

Device fabrication

Glass microscope slides (1 mm thick) were cut into 1"×1" squares using a diamond tip pen and cleaned. The substrates were first rinsed with acetone and then bath sonicated in acetone for 10 min. This process was then repeated using isopropanol. Finally, the substrates were rinsed with deionized water, dried with compressed air, and allowed to further dry in an oven at 100 °C to remove any remaining moisture. After cleaning, the substrates were secured with patterning masks and placed into a thermal evaporator where a 50 nm Al gate was applied. These Al-coated glass slides act as the first part of all of the devices considered in this work.

For the 50 nm cPVP and cPVP + CFO thick films in MIM and FET structures, we started by making a stock solution of 5wt% PVP + 2.5wt% PMMF in PGMEA, which was heated at 80 °C for 1 h and stirred overnight. 6 mg of neat CFO was dispersed into 500 µL PGMEA and horn tip sonicated at 10 kHz for 45 s. The stock PVP solution (~ 80 mg/mL) was divided into two parts, 500 µL each. One part was mixed with 500 µL PGMEA to form the pure cPVP solution (~ 40 mg/mL) and the other part was combined with the CFO dispersion (~ 40 mg/mL cPVP, ~ 6 mg/mL CFO). Each solution was spincoated onto the glass substrates (patterned with the Al gate) at 5000 RPM for 60 s and the films were then immediately annealed at 120 °C for 1 h to facilitate crosslinking. Both the spincoating and annealing were performed under a nitrogen atmosphere. Finally, 50 nm Au contacts were thermally evaporated on top of the cPVP or cPVP + CFO film using a patterning mask which produced MIM structures with pads of varying cross-sectional area. The Au contacts for MIM and MIS devices were circular and varied in diameter from 250 to 1000 µm. The process was the same for the pentacene FET architectures, but a mask was used during the Al and pentacene evaporations so as to restrict the gate and semiconductor channel to a thin line in the center of the device. The evaporated Au contacts used a different mask such that devices with varying W/L ratio were achieved for the FET architectures. Each device had a channel width of 1000 µm and the channel length varying from 50 to 125 µm.

When utilizing the PVA-coated CFO nanocrystals dispersed in DMF, a cPVP stock solution was made using DMF as the solvent instead of PGEMA. The CFO dispersion was mixed with the cPVP stock solution in a 1:1 ratio by volume, resulting in a final mixture which had a concentration of 60 mg/mL in cPVP and 3 mg/mL CFO. This mixture was spincoated onto Al-coated glass and annealed using the same parameters as before. From

there 50 nm of pentacene was evaporated onto the surface of the film, followed by 50 nm of patterned Au contacts to form the MIS structures. For the FET structures, the same patterning masks were used as previously mentioned for the neat CFO structures.

Characterization

TEM: The morphology of CFO nanocrystals and CFO nanocrystals coated by PVA was characterized using transmission electron microscopy (TEM, FEI Tecnai-20). TEM specimens were prepared by dropping 10 µl of CFO nanocrystals solution (dispersed in Heptane) and CFO nanocrystals coated by PVA solution (dispersed in DMF) solution, on a carbon-coated copper grid (Ted Pella) and drying solution. TEM imaging was conducted at 200 kV.

TGA: The weight ratio of the organic compounds (oleic acid and PVA) to the CFO nanocrystals was measured by thermal gravimetric analysis (TGA). Dried CFO nanocrystals and CFO nanocrystals coated by PVA were mounted on a TGA pan (Initial weight: 10 mg). The TGA (SDT-Q600, TA Instruments) was carried out in helium by heating the sample at a rate of 10 °C/min from room temperature to 600 °C. The 10 mg of pure PVA was conducted using the same procedure.

XRD: The X-ray diffraction (XRD) pattern of CFO nanocrystals was obtained on a Rigaku desktop X-ray diffractometer using CuKα (1.54059 Å) radiation with the X-ray generator operating at 20 kV and 30 mA. Data were collected for a 2θ range of 15–100° at an angular resolution of 0.01°/s with 0.02° step.

C–V & C–F: The MIM and MIS devices discussed in this paper were characterized using a Hewlett Packard 4248A LCR meter. From here we were able to measure the devices' capacitance as the frequency of the signal was swept from 1 kHz to 1 MHz. For the MIS structures, we determined the C–V characteristics by sweeping the applied DC voltage and measuring the change in the capacitance of the device while the frequency was held constant. For these measurements, the frequency was held at a low value (usually between 1 and 5 kHz) so the results could be used to predict the behavior of our FET devices (which were measured using only DC voltages).

From the capacitance versus frequency/voltage-dependent characteristics, we determined the average capacitance per unit area and from there calculate the thickness of our cPVP dielectric films by using the following relationship:

$$C_A = \frac{\kappa \varepsilon_0}{t},$$

where C_A is the capacitance per unit of cross-sectional area of the device pad, κ is the dielectric constant for cPVP (≈ 4), ε_0 is the permittivity of free space, and t is the thickness of the film.

The C–V characteristics provided insights into the hysteresis present within the MIS devices as well as the biases at which the charges saturated in the semiconductor layer. This latter detail outlined the operating voltages for the FET devices, which were all low (< 10 V).

FET I–V Characteristics: The transfer and output characteristics of the FET devices used both Keithley 2400 and Keithley 236 sourcemeters, with the measurement sequence controlled by LabView programs. From the output characteristics, in which the I_{DS} is measured as the drain-source bias is swept for differing constant gate biases, we could determine the linear and saturation regimes of FET device operation.

For the devices containing CFO nanoparticles (either neat or the PVA-coated nanocrystals), the C–V, C–F, and transfer and output measurements were repeated while the devices were attached to a magnet. The orientation of the substrate with was such that the magnetic field would be oriented parallel to the electric field produced by the gate during device operation.

Acknowledgments

Author Contributions

The manuscript was written through contributions of all authors. All authors have given approval to the final version of the manuscript.

Data Availability

The data will be made available upon reasonable request from the corresponding author (S.G).

Declarations

Conflict of interest On behalf of all authors, the corresponding author states that there is no conflict of interest. The data will be made available upon reasonable request.

References

1. K. Liu, B. Ouyang, X. Guo, Y. Guo, Y. Liu, npj Flex. Electron. **6**, 1 (2022)
2. T. Someya, Z. Bao, G.G. Malliaras, Nature **540**, 379 (2016)
3. S.-T. Han, H. Peng, Q. Sun, S. Venkatesh, K.-S. Chung, S.C. Lau, Y. Zhou, V.A.L. Roy, Adv. Mater. **29**, 1700375 (2017)
4. S. Fratini, M. Nikolka, A. Salleo, G. Schweicher, H. Sirringhaus, Nat. Mater. **19**, 491 (2020)
5. H. Chen, W. Zhang, M. Li, G. He, X. Guo, Chem. Rev. **120**, 2879 (2020)
6. J. Veres, S.D. Ogier, S.W. Leeming, D.C. Cupertino, S. Mohialdin Khaffaf, Adv. Funct. Mater. **13**, 199 (2003)
7. T. Richards, M. Bird, H. Sirringhaus, J. Chem. Phys. **128**, 234905 (2008)
8. A. Laudari, S. Guha, J. Appl. Phys. **117**, 105501 (2015)
9. I.N. Hulea, S. Fratini, H. Xie, C.L. Mulder, N.N. Iossad, G. Rastelli, S. Ciuchi, A.F. Morpurgo, Nat Mater **5**, 982 (2006)
10. H. Houili, J.D. Picon, L. Zuppiroli, M.N. Bussac, J. Appl. Phys. **100**, 023702 (2006)
11. A. Laudari, A.R. Mazza, A. Daykin, S. Khanra, K. Ghosh, F. Cummings, T. Muller, P.F. Miceli, S. Guha, Phys. Rev. Appl. **10**, 014011 (2018)
12. A. Laudari, A. Pickett, F. Shahedipour-Sandvik, K. Hogan, J.E. Anthony, X. He, S. Guha, Adv. Mater. Interfaces **6**, 1801787 (2019)
13. J.-H. Lee et al., Nat. Med. **13**, 95 (2007)
14. K. Maaz, A. Mumtaz, S.K. Hasanain, A. Ceylan, J. Magn. Magn. **308**, 289 (2007)
15. S.M. Ansari, K.C. Ghosh, R.S. Devan, D. Sen, P.U. Sastry, Y.D. Kolekar, C.V. Ramana, ACS Omega **5**, 19315 (2020)
16. Y.-W. Jun, J.-W. Seo, J. Cheon, Acc. Chem. Res **41**, 179 (2008)
17. N. Sanpo, C.C. Berndt, C. Wen, J. Wang, Acta Biomater. **9**, 5830 (2013)
18. S. Amiri, H. Shokrollahi, Mater. Sci. Eng. C **33**, 1 (2013)
19. J. Gallo, N.J. Long, E.O. Aboagye, Chem. Soc. Rev. **42**, 7816 (2013)
20. J.H. Jung, S. Kim, H. Kim, J. Park, J.H. Oh, Small **11**, 4976 (2015)
21. Y. Zang, F. Zhang, D. Huang, C.-A. Di, D. Zhu, Adv. Mater. **27**, 7979 (2015)
22. S. Khanra, M. Abdullah-Al Mamun, F.F. Ferreira, K. Ghosh, S. Guha, ACS Appl. Nano Mater. **1**, 1175 (2018)
23. X. Zeng et al., Nanoscale **9**, 7493 (2017)
24. S.E. Shirsath, D. Wang, J. Zhang, A. Morisako, S. Li, X. Liu, ACS Appl. Electron. Mater. **2**, 3650 (2020)
25. S. Sun, H. Zeng, D.B. Robinson, S. Raoux, P.M. Rice, S.X. Wang, G. Li, J. Am. Chem. Soc. **126**, 273 (2004)
26. N.B. Ukah, J. Granstrom, R.R. Sanganna Gari, G.M. King, S. Guha, Appl. Phys. Lett. **99**, 243302 (2011)
27. N.B. Ukah, S.P. Senanayak, D. Adil, G. Knotts, J. Granstrom, K.S. Narayan, S. Guha, J. Polym. Sci. B Polym. Phys. **51**, 1533 (2013)
28. G. Knotts, A. Bhaumik, K. Ghosh, S. Guha, Appl. Phys. Lett. **104**, 233301 (2014)
29. A. Laudari, J. Barron, A. Pickett, S. Guha, A.C.S. Appl, ACS Appl. Mater. Interfaces **12**, 26757 (2020)
30. K.T. McCarthy, A.F. Hebard, S.B. Arnason, Phys. Rev. Lett. **90**, 117201 (2003)
31. G. Catalan, D. O'Neill, R.M. Bowman, J.M. Gregg, Appl. Phys. Lett. **77**, 3078 (2000)

32. N.S. Negi, K. Bala, A. Yadav, R.K. Kotnala, J. Appl. Phys. **117**, 164101 (2015)

33. H. Zang, J. Wang, M. Li, L. He, Z. Liu, D. Zhang, B. Hu, J. Phys. Chem. B **117**, 14136 (2013)

34. S. Lee, B. Koo, J. Shin, E. Lee, H. Park, H. Kim, Appl. Phys. Lett. **88**, 162109 (2006)

35. S.C. Lim, S.H. Kim, J.B. Koo, J.H. Lee, C.H. Ku, Y.S. Yang, T. Zyung, Appl. Phys. Lett. **90**, 173512 (2007)

36. M.R. Beaulieu, J.K. Baral, N.R. Hendricks, Y. Tang, A.L. Briseño, J.J. Watkins, ACS Appl. Mater. Interfaces **5**, 13096 (2013)

37. Y. Zhou, S.-T. Han, Z.-X. Xu, X.-B. Yang, H.-P. Ng, L.-B. Huang, V.A.L. Roy, J. Mater. Chem. **22**, 14246 (2012)

38. Y. Zhou, S.-T. Han, Z.-X. Xu, V.A.L. Roy, J. Mater. Chem. **22**, 4060 (2012)

39. J. Kim, S.H. Lim, Y.S. Kim, J. Am. Chem. Soc. **132**, 14721 (2010)

40. J. Kim, J. Kim, Y. Seol, T. Kim, N.-E. Lee, J. Nanosci. Nanotechnol. **16**, 11335 (2016)

41. B. Canimkurbey, Ç. Çakirlar, S. Piravadili Mucur, M. Yasin, S. Berber, J. Mater. Sci. **30**, 18384 (2019)